

# Quantiles as Robust Probes of Non-Gaussianity in 21-cm Images

Alon Banet<sup>1\*</sup>, Rennan Barkana<sup>1</sup>, Anastasia Fialkov<sup>2</sup>, Or Guttman<sup>1</sup>,

<sup>1</sup> *School of Physics and Astronomy, Tel Aviv University, Tel Aviv 69978, Israel*

<sup>2</sup> *Institute of Astronomy, University of Cambridge, Madingley Road, Cambridge CB3 0HA, UK*

13 February 2020

## ABSTRACT

The early epoch in which the first stars and galaxies formed is among the most exciting unexplored eras of the Universe. A major research effort focuses on probing this era with the 21-cm spectral line of hydrogen. While most research focused on statistics like the 21-cm power spectrum or the sky-averaged global signal, there are other ways to analyze tomographic 21-cm maps, which may lead to novel insights. We suggest statistics based on quantiles as a method to probe non-Gaussianities of the 21-cm signal. We show that they can be used in particular to probe the variance, skewness, and kurtosis of the temperature distribution, but are more flexible and robust than these standard statistics. We test these statistics on a range of possible astrophysical models, including different galactic halo masses, star-formation efficiencies, and spectra of the X-ray heating sources, plus an exotic model with an excess early radio background. Simulating data with angular resolution and thermal noise as expected for the Square Kilometre Array (SKA), we conclude that these statistics can be measured out to redshifts above 20 and offer a promising statistical method for probing early cosmic history.

**Key words:** dark ages, reionization, first stars – cosmology: theory – galaxies: high redshift

## 1 INTRODUCTION

Ever since Penzias and Wilson discovered the Cosmic Microwave Background (CMB) in 1964, cosmologists have had a good understanding of the Universe in its early stages. Meanwhile, modern telescopes have allowed astronomers to study astronomical objects in the more recent Universe, reaching times as early as a billion years after the Big Bang. Despite tremendous progress in recent decades, the exciting period in between, in which stars and galaxies first formed and evolved, remains largely unobserved to this day.

While a few bright galaxies that date back to 400 Myr after the Big Bang have been detected directly via telescopes, it is thought that most of the early stars are distributed in a large number of very small galaxies, making them difficult to observe directly. The most promising probe of these early times is the spin-flip transition of neutral hydrogen. Since redshift acts as the line-of-sight dimension, it can be used to produce a 3-D tomography map of the cosmic gas.

The brightness temperature of the 21-cm signal (which is measured relative to the CMB temperature) is determined

by the spin temperature, which denotes the abundance of the excited level of the hyperfine split of hydrogen relative to the ground level. The spin temperature is affected by astrophysical and cosmological events, so therefore it may allow us to study star and galaxy formation within dark matter halos, as well as phenomena like cosmic reionization and early cosmic heating.

Previous studies have shown that the 21-cm signal should have large spatial fluctuations, which stem not only from reionization at low redshifts, but also from fluctuations in the Ly $\alpha$  intensity during the Ly $\alpha$  coupling era (Barkana & Loeb 2005) and fluctuations in the X-ray background during the era of cosmic heating (Pritchard & Furlanetto 2007). Research over this past decade has focused on the statistics of these fluctuations and in particular, on the 21-cm power spectrum, a highly promising measure of the 21-cm signal. Since the foregrounds are expected to have a smooth spectrum, the power spectrum may be measured in the near future. Another approach, pursued by both theorists and experimentalists is the sky-averaged global 21-cm signal, which could prove useful in independently constraining the parameters of the early universe. The first claimed detection of a cosmological 21-cm signal is of the global signal at cosmic dawn, by the EDGES experiment (Bowman et al. 2018). The

\* E-mail: alon.banet@gmail.com

surprisingly-deep absorption, if confirmed, would require an exotic explanation, such as an interaction with dark matter that cools the baryons (Barkana 2018), or an enhanced early radio background (discussed further below).

These methods span only part of the richness the 21-cm signal holds. In particular, they are not able to probe non-Gaussianities in the signal caused by the non-linear processes described above. In the near future the Square Kilometre Array (SKA) should provide a detailed 3-D map of the 21-cm fluctuation signal. However, the topic of analyzing such images has received only limited attention (Koopmans et al. 2015). The aim of this study is to explore new ways of studying these maps, in order to gain new insights about the 21-cm signal. In the near future, maps will likely have a fairly low signal-to-noise ratio, so use of averaging through statistics will be necessary, but it is possible to go beyond the power spectrum. Use of the 21-cm bispectrum has been explored (e.g., Bharadwaj & Pandey 2005; Majumdar, et al. 2018; Trott, et al. 2019). A number of papers have explored use of the probability distribution function of 21-cm brightness temperature (e.g., Ciardi & Madau 2003; Furlanetto, Zaldarriaga & Hernquist 2004; Mellema, et al. 2006; Ichikawa, et al. 2010; Mondal, et al. 2015), and in particular the skewness and kurtosis statistics, mostly during the reionization era (Wyithe & Morales 2007; Harker, et al. 2009; Watkinson & Pritchard 2014; Kubota, et al. 2016; Kitiwisit, et al. 2016) and out to cosmic dawn (Shimabukuro, et al. 2015; Watkinson & Pritchard 2015). We explore these standard statistics within a wide range of possible models, and also suggest new statistics that serve as a more robust and flexible measure of non-Gaussian characteristics and can help us explore the evolution of the signal and understand the processes affecting it.

This paper is structured as follows. In section 2 we present the details of how we simulated 21-cm images, laying out the assumed models and their main parameters (2.1), and how we imitated observational aspects corresponding to resolution and noise (2.2). In section 3 we present our statistical methods and results, laying out measures based on quantiles (3.1), finding average radial profiles (3.2), showing how we corrected for thermal noise (3.3), plotting the variance and our alternative (the quantile average) (3.4), exploring the extra flexibility of the quantile average (3.5), plotting the skewness and our alternative (the quantile difference) (3.6), as well as the kurtosis and our alternative (the normalized quantile average) (3.7). Finally, we summarize and conclude in section 4.

## 2 SIMULATED 21-CM TOMOGRAPHY MAPS

We obtain the 21-cm image boxes using a semi-numerical simulation (e.g., Mesinger, Furlanetto & Cen 2011) in a box that is 384 Mpc on a side, with 3 Mpc resolution (comoving units), as described by Cohen et al. (2017). The observed brightness temperature (relative to the CMB) depends on the spin temperature  $T_s$ , the neutral fraction  $x_{\text{HI}}$ , and the baryonic overdensity  $\delta$ , as follows (e.g., Madau, Meiksin & Rees 1997; Barkana 2016):

$$T_b \propto x_{\text{HI}}(1 + \delta) \left( 1 - \frac{T_{\text{CMB}}}{T_s} \right). \quad (1)$$

The spin temperature plays an important role in the evolution of the signal, and  $T_s$  can be expressed as a weighted mean (Barkana 2016):

$$T_s^{-1} = \frac{T_{\text{CMB}}^{-1} + x_c T_k^{-1} + x_\alpha T_c^{-1}}{1 + x_c + x_\alpha}, \quad (2)$$

where  $T_k$  is the kinetic temperature of the gas,  $T_c$  is the effective (color) Ly $\alpha$  temperature (which is very close to  $T_k$ ), and  $x_c$ ,  $x_\alpha$  are the coupling coefficients for collisions and Ly $\alpha$  scattering, respectively.

At redshifts above  $z \sim 200$ ,  $T_k$  was close to  $T_{\text{CMB}}$ , causing the signal to vanish. As the universe expanded the gas cooled adiabatically, faster than the CMB, while atomic collisions kept the spin temperature coupled to  $T_k$ , leading to an absorption signal. Eventually, the gas density decreased enough to make collisional coupling ineffective, the radiative coupling of  $T_s$  to  $T_{\text{CMB}}$  dominated and the signal diminished. As star formation began, Ly $\alpha$  photons were emitted and coupled  $T_s$  to  $T_k$  via the Wouthuysen-Field (Wouthuysen 1952; Field 1958) effect. Meanwhile, X-ray sources started heating the cosmic gas and UV photons ionized the gas around galaxies, creating ionized bubbles and initiating the process of cosmic reionization. It is useful to define three milestone redshifts. A typical theoretical set of definitions would be: Ly $\alpha$  coupling, defined as when the mean  $x_\alpha = 1$ ; the heating transition, defined as when the mean  $T_k = T_{\text{CMB}}$ ; and the mid-point of reionization, at which the mean  $x_{\text{HI}} = 0.5$ . However, in plots below we adopt a modified set of milestone redshifts, defined phenomenologically using peak redshifts of our main measure of the signal (the quantile average, discussed below in section 3.4 and shown for our various models in Figure 4).

### 2.1 Models and parameters

To illustrate our method of exploring the characteristics of 21-cm intensity maps, we used several models that differ in their input astrophysical parameters. Given the early state of 21-cm observations, the details of astrophysics at high redshift are still highly uncertain, and it is important to consider a wide range of possible models. The following are the main parameters of our models (Cohen et al. 2017):

(i) Star formation efficiency (SFE) - the fraction of gas that is converted into stars, out of the gas that falls into star-forming dark matter halos. The overall SFE depends on the details of the process of star formation as well as the dominant feedback mechanisms. It strongly affects the 21-cm signal by influencing the amount of radiation produced by stars. For otherwise identical astrophysical parameters, a higher SFE implies an earlier onset of Ly $\alpha$  coupling, and a faster build-up of X-ray and ionizing radiation backgrounds; hence, a high SFE value shifts the cosmological 21-cm signal milestones to higher redshifts.

(ii) Cooling mass - the minimum halo mass in which there is significant gas cooling (and thus star formation). It depends on the cooling channels of the gas in halos, and is best described in terms of a minimum circular velocity  $V_c$ . In atomic cooling halos, stars form with masses down to the cooling threshold of atomic hydrogen, given by  $V_c = 16.5 \text{ km s}^{-1}$ . As an example of strong feedback, we consider a model of ‘‘Massive’’ halos in which stars only form

in halos with masses of at least 100 times the mass required for atomic cooling, which corresponds to  $V_c = 76.5 \text{ km s}^{-1}$ . In this model star formation is delayed, so that the 21-cm milestones are shifted to lower redshift values.

(iii) The spectrum of early X-ray sources. The mean free path of an X-ray photon is proportional to  $E_{\text{photon}}^3$ , and thus soft X-rays have relatively short mean free paths and therefore they are absorbed soon after emission, heating the local gas before suffering significant energy loss due to redshift effects. Thus, soft X-ray sources cause large spatial fluctuations in the gas temperature during cosmic heating. However, the most plausible sources of cosmic heating are X-ray binaries, which are expected to have a relatively hard spectrum (Mirabel et al. 2011; Fragos, et al. 2013). Due to their long mean free path, the photons emitted from such sources will be absorbed late, after having lost a significant part of their energy as a result of cosmological redshift (Fialkov et al. 2014). Hence, a hard X-ray spectrum leads to cosmic heating at a later time and reduces the fluctuations in  $T_k$ . Our standard assumption is a hard X-ray spectrum, but given the current uncertainty in the properties of high-redshift sources, we also consider a model with a soft X-ray spectrum.

(iv) X-ray radiation efficiency - proportional to the ratio of the X-ray luminosity to the star formation rate (SFR). It is normalized so that unity corresponds to low metallicity, low redshift starburst galaxies (Mineo et al. 2012). Higher X-ray efficiency leads to earlier cosmic heating.

(v) Excess radio background radiation. In order to explain the EDGES measurement of the global 21-cm signal at  $z = 17.2$  (which corresponds to  $\nu = 78.2 \text{ MHz}$ ) (Bowman et al. 2018), we consider an example of an exotic model with a greatly enhanced early radio background (Bowman et al. 2018; Feng & Holder 2018; Fialkov & Barkana 2019). In this model the background temperature at redshift  $z$  is modified to:

$$T_{\text{rad}} = T_{\text{CMB}}(1+z) \left[ 1 + A_r \left( \frac{\nu_{\text{obs}}}{78 \text{ MHz}} \right)^\beta \right], \quad (3)$$

where  $\nu_{\text{obs}}$  is the observed frequency,  $A_r$  is the amplitude defined relative to the CMB temperature, and  $\beta = -2.6$  is the spectral index, assumed to follow the shape of the observed radio background. The radio background enhances the 21-cm signal when there is absorption, i.e., when  $T_s \ll T_{\text{rad}}$ .

For our study we chose four models from Cohen et al. 2017 plus an exotic model with an excess radio background, chosen to be generally consistent with the EDGES measurement (Fialkov & Barkana 2019). The full parameters are listed in Table 1.

## 2.2 Angular resolution, thermal noise, and smoothing

We generated mock signals that correspond to observations with the SKA (i.e., the low-frequency instrument of the phase-one SKA), in terms of various resolutions and the expected thermal noise for each. It is interesting to consider various resolutions (not only the highest achievable SKA resolution) since low resolution images have significantly lower

Model	$f_*$	$f_X$	SED	Halo type
Standard #53	0.05	1	Hard	Atomic cooling ( $V_c = 16.5 \text{ km/s}$ )
Low-Efficiency #37	0.005	0.1	Hard	Atomic cooling
Soft #55	0.05	1	Soft	Atomic cooling
Massive #186	0.5	0.1	Hard	Massive ( $V_c = 76.5 \text{ km/s}$ )
Radio	0.05	1	Hard	Atomic cooling

**Table 1.** Parameters of the models that we consider: star formation efficiency  $f_*$ , X-ray efficiency of X-ray sources  $f_X$ , spectral energy distribution (SED) of X-ray sources, and minimum circular velocity  $V_c$ . The first four models are taken from Cohen et al. (2017) [case numbers from there are indicated]; these all have a total CMB optical depth  $\tau = 0.066$ . The Radio model has a radio background amplitude  $A_r = 4.2$  (measured at the central EDGES frequency of 78 MHz, and corresponding to 0.22% of the CMB at 1.42 GHz) and  $\tau = 0.0737$ .

noise. To create these mock 21-cm maps, we used the following procedure [Koopmans et al. (2015); also L. Koopmans, personal communication].

We adopted the reasonable approximation of a Gaussian point-spread function (PSF). Thus we used the 3 Mpc voxels (i.e., 3-D pixels) in our simulation box but for each resolution we smoothed the signal map with a two-dimensional Gaussian with full-width at half max (FWHM) of  $2R$ , where  $R$  is the smoothing radius. We illustrate our results with three values of  $R$ , 10, 20, and 40 Mpc. In terms of the telescope array, the FWHM corresponds to  $\sim 0.6\lambda/D$ , where  $\lambda$  is the wavelength and  $D$  is the diameter within which baselines are included. Different resolutions correspond to using different values of  $D$ , so the dependence of the noise on the resolution depends on the distribution of baselines. In the frequency direction, the voxel size was always fixed at 3 Mpc. Now, the PSF also indicates how the thermal noise is correlated in the image. To produce a realistic noise map, we first generated a map of independent Gaussian random variables in each voxel with  $\sigma = 1$ . We then smoothed (each slice of) the map using the same two-dimensional Gaussian with FWHM  $2R$ , which gave the correct angular correlations. The map was then rescaled so that each slice has the expected root mean square (RMS) value of the noise for the SKA, which depends on the redshift and the smoothing radius  $R$  approximately as [Koopmans et al. (2015); also L. Koopmans, personal communication]:

$$\sigma_{\text{thermal}} = \begin{cases} a \left( \frac{1+z}{17} \right)^b & \text{if } z \leq 16, \\ a \left( \frac{1+z}{17} \right)^c & \text{otherwise,} \end{cases} \quad (4)$$

where  $a$ ,  $b$  and  $c$  are the numerical coefficients for each smoothing radius given in Table 2 (assuming a 1000 hr integration by the SKA). Finally, the resulting noise map was added to the signal.

A given resolution corresponds to 2-D Gaussian smoothing with a radius  $R$ , but it is also useful to consider applying additional 3-D smoothing as a step in the

$R$ [Mpc]	10	20	40
$a$ [mK]	15	4.0	1.8
$b$	3.1	2.7	2.8
$c$	4.7	5.1	4.2

**Table 2.** The numerical coefficients for each smoothing radius, for thermal noise of the SKA as given by Equation 4.

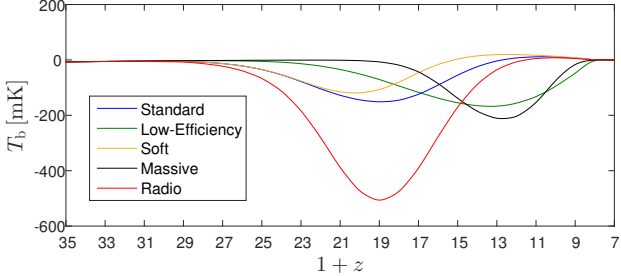


**Figure 1.** The global 21-cm signal as a function of redshift for our five models, Standard (blue), Low-Efficiency (green), Soft (orange), Massive (black), and Radio (red).

data analysis. The idea is to produce a more isotropic image, which is more conducive for measuring statistics that are designed to probe spherically-averaged structure. Now, while any smoothing removes some information in the map, it also smooths out and thus lowers the thermal noise. In our results below, we have found that the differences are small between using the images with or without 3-D smoothing, but in most cases the 3-D smoothing increases the signal-to-noise ratio, i.e., the noise is smoothed-out more than the signal. This makes sense since the typical coherence/correlation scale of the noise is  $R$  (due to the PSF), while the typical scales of the 21-cm features (due to reionization, heating, or Ly $\alpha$  coupling) are usually significantly larger. Thus as our default procedure we did include 3-D smoothing, using a spherical top-hat with the same smoothing radius  $R$  as in the corresponding 2-D Gaussian.

### 3 STATISTICAL METHODS AND RESULTS

We first show the sky-averaged (global) signal for all five models from Table 1 as predicted from the simulation. All five curves show the same general behavior of a deep absorption dip, as is the case for all reasonable models (Cohen et al. 2017). Three models are especially similar in their timing: the Standard, Soft, and Radio models have relatively early Ly $\alpha$  coupling and X-ray heating, resulting in a peak absorption at  $z \sim 18 - 19$ , followed by a rise to emission ( $T_b > 0$ ) before the drop to zero due to reionization. On the other hand, the Low-Efficiency and Massive models have much later star formation, so that Ly $\alpha$  coupling is delayed and X-ray heating overlaps with reionization and does not manage to lead to emission. Comparing the Soft model to the Standard one, the heating phase starts earlier in the Soft model, leading to an earlier rise from the absorption trough. The Radio model has a very deep Ly $\alpha$  minimum due to the excess radio background.

### 3.1 Histograms and quantiles

Our statistical tools are mostly based on histograms of the 21-cm signal map, i.e., the probability distribution function  $p(T_b)$  of the 21-cm intensity (brightness temperature  $T_b$ ) in voxels, normalized to a total area of unity. As the variable we use  $\Delta T_b$ , which is  $T_b$  measured relative to the mean temperature at the same redshift, since interferometers do not measure the zero point. Figure 2 shows two examples of such histograms for separate models and cosmic times. The distributions are clearly non-Gaussian, and one of the main features we focus on is the obvious asymmetry. The shape of the asymmetry depends in a complex way on the astrophysical processes and parameters; these examples illustrate opposite signs of the skewness.

In what follows, we use the cumulative distribution function (CDF) of the signal, either the upper portion:

$$F_+(\Delta T_b) \equiv \int_{\Delta T_b}^{\infty} p(\Delta \hat{T}_b) d\Delta \hat{T}_b, \quad (5)$$

or the lower portion:

$$F_-(\Delta T_b) \equiv \int_{-\infty}^{\Delta T_b} p(\Delta \hat{T}_b) d\Delta \hat{T}_b. \quad (6)$$

Note that  $F_+(-\infty) = F_-(\infty) = 1$ . We measure characteristic brightness temperatures as thresholds at certain values of the CDF. This is the inverse function of the CDF (also called the quantile function  $Q$ , which here has units of mK). For a given fraction  $f$  of the total probability, we have an upper threshold  $Q_+(f)$  so that a fraction  $f$  of the probability lies at temperatures above  $Q_+(f)$ , and similarly a lower threshold  $Q_-(f)$ . They are defined so that

$$F_+(Q_+(f)) = f, \quad (7)$$

and

$$F_-(Q_-(f)) = f. \quad (8)$$

For the probability fractions we use characteristic thresholds  $t$  based on the cumulative probability of a normal distribution, measured in units of the standard deviation  $\sigma$ . For instance, we define  $Q(t = 1\sigma) \equiv Q(f = 15.9\%)$ , where this holds for both  $Q_+$  and  $Q_-$ . Note that  $Q_+$  and  $Q_-$  are defined to be one-sided so we use the corresponding one-sided fractions of a Gaussian (e.g.,  $f = 15.9\%$  for  $t = 1\sigma$ , not  $f = 31.7\%$ ). More generally, the relation between  $f$  and  $t$  is given by

$$f(t) = \frac{1}{2} \operatorname{erfc} \left( \frac{t}{\sqrt{2}} \right), \quad (9)$$

where  $t$  is measured in units of  $\sigma$ . Table 3 lists the values of various thresholds that we use below along with their corresponding percentiles, according to eq. 9. Note that for a Gaussian distribution,  $Q_+(t) = -Q_-(t) = t\sigma$ .

Quantiles for one case are shown in the right panel of Figure 2. In this case,  $Q_+$  and  $Q_-$  have nearly the same magnitude at  $1\sigma$ ; while  $Q_-$  is closer than  $Q_+$  to the peak of the PDF as well as to its median, we have defined  $Q_+$  and  $Q_-$  as they are measured in 21-cm images, i.e., relative to the cosmic mean brightness temperature. At the  $2\sigma$  threshold the difference becomes clear, with the higher  $|Q_+|$  reflecting the broader tail at high brightness temperature. In the Low-Efficiency model shown here during reionization, the

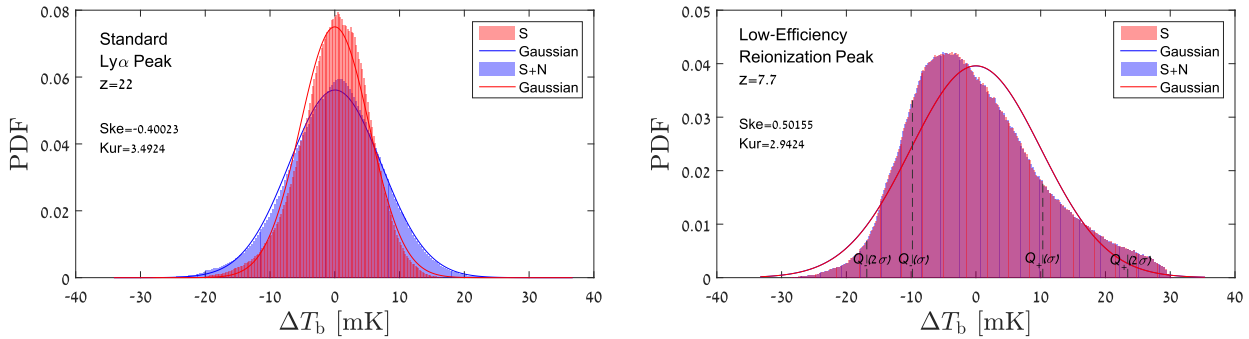


**Figure 2.** Probability distribution functions (PDFs) of the noiseless signal (peach histogram; red curve) and the signal with added noise (light blue histogram; blue curve), assuming an  $R = 20$  Mpc angular resolution (plus 3-D smoothing). Each solid curve corresponds to a Gaussian PDF with the same mean and variance as the histogram with matching color, for comparison. Left panel: Standard model at the Ly $\alpha$  peak (for definitions of the various peaks, see section 3.4 below). Right panel: Low-Efficiency model at the Reionization peak. The skewness and kurtosis values of the signal-only histograms are also noted; these measures are discussed in detail in the last two subsections of section 3. The added SKA thermal noise is discussed in section 2.2. In the right panel, the quantiles  $Q_+$  and  $Q_-$  are shown for the signal, for  $t = 1\sigma$  as well as  $t = 2\sigma$ . Note that in the right panel the noise is negligible due to the lower redshift, making the two histograms in it nearly identical.

$t$	$f(t)$	$1 - f(t)$	$N_{\text{vx}}$
$0.5\sigma$	30.9%	69.1%	647,000
$1\sigma$	15.9%	84.1%	333,000
$1.5\sigma$	6.7%	93.3%	140,000
$2\sigma$	2.28%	97.72%	47,700
$2.5\sigma$	0.62%	99.38%	13,000
$3\sigma$	0.135%	99.865%	2,830

**Table 3.** List of thresholds used in this paper along with the corresponding percentiles of the normal distribution.  $N_{\text{vx}}$  denotes the actual number of voxels corresponding to the fraction  $f(t)$ , for a  $128^3$  voxel simulation box as used here.

intergalactic medium is still cold, so that the high  $T_b$  tail corresponds to regions that are mostly reionized (though not completely so, due to the smoothing of the map, which mixes ionized bubbles with nearby pixels that are still partly neutral).

### 3.2 Radial profiles

In most of our analysis below, we focus on the PDF of  $T_b$  values and various derived statistics as laid out in the previous subsection. This approach brings out non-Gaussianity most clearly, and makes thermal noise especially easy to deal with. However, there is additional spatial information that can be derived from the 21-cm map. We briefly give an example of this here.

We can use the thresholds to explore what roughly corresponds to radial profiles around temperature peaks. Specifically, we found the average profiles around the voxels with the highest or lowest values of  $\Delta T_b$ . From this we can examine the contribution of various spatial scales to the fluctuations and also look for asymmetry (and thus non-Gaussianity) by comparing the highest and lowest voxels. Since we wanted average spherical profiles, in order to select the voxels we used as before the 3-D spherically averaged  $T_b$  around each voxel. As an example, we chose  $R = 20$  Mpc and used the 15.9% highest and lowest voxels (corresponding

to  $t = 1\sigma$  in the previous subsection). To find the profiles, at each distance  $r$  we found the volume-averaged smoothed signal in the shell that includes points at distances between  $r - R$  and  $r + R$  from the central voxel. For  $r = 0$  we simply used the spherical average out to radius  $R$ . Finally, the profiles of each group (highest or lowest pixels) were stacked to produce an average profile for each group. Figure 3 illustrates the resulting profiles (shown normalized, relative to  $r = 0$ ) for all five models at the Ly $\alpha$  peak. Differences between the profiles of the highest and lowest pixels are visible for all models, i.e., there is clear asymmetry. Also, different models show different characteristic scales for the drop of the profile. For example, the profile that declines most slowly (i.e., shows the strongest large-scale correlations) corresponds to the Massive model, where the halos are massive, rare, and more highly biased than in the other models.

### 3.3 Quantiles and noisy maps

From here on, we consider the quantiles at various thresholds as defined in section 3.1. At each threshold level  $t$ , we find  $Q_+(t)$  and  $Q_-(t)$ , which measure the brightness temperature above or below the mean which describes a fraction of the map corresponding to that threshold. These quantities probe the magnitude of the positive and negative fluctuations, and the choice of  $t$  gives us controls: a higher threshold  $t$  corresponds to probing rarer fluctuations, while a lower threshold is more robust and less sensitive to noise, especially to outliers in the data. Standard statistical measures average over the entire distribution and do not offer such flexibility. As we show, we can reconstruct the standard non-Gaussian statistics with quantiles, plus look for additional measures.

For a Gaussian distribution, a quantile at a given threshold value would give a brightness temperature that is a fixed multiple of the standard deviation  $\sigma$  of the distribution. Thus, in general, what a quantile measures is roughly (a multiple of) the standard deviation. Now, in general, the total variance of the noisy signal equals the sum of the signal variance and noise variance (assuming that they are independent). This leads us to use a simple procedure for cor-

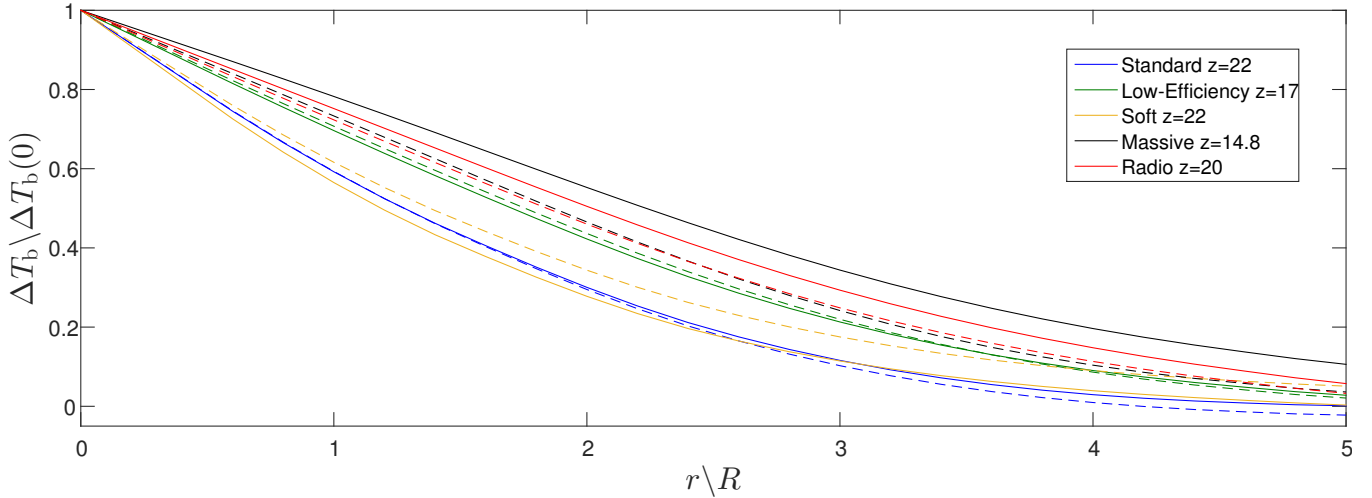


**Figure 3.** Normalized radial  $T_b$  profiles for the various models (Table 1), with  $R = 20$  Mpc and at redshifts corresponding to the Ly $\alpha$  peak (for definitions of the various peaks, see section 3.4 below). Standard - blue, Low-Efficiency - green, Soft - orange, Massive - black, Radio - red. Solid lines show the average profile around the 15.9% highest voxels in the map, and dashed lines show the average profile around the 15.9% lowest voxels.

recting the measured quantiles from our mock data for the effect of noise. The estimated signal is taken as

$$S_{\text{est}} = \sqrt{(S + N_1)^2 - N_2^2}, \quad (10)$$

where  $S_{\text{est}}$  refers to the estimated signal (either  $Q_+$  or  $Q_-$  at some threshold  $t$ ),  $S + N_1$  is the measured signal from a 21-cm image with signal plus thermal noise, and  $N_2$  is the same quantity measured from a noise-only 21-cm image, using noise  $N_2$  generated independently from  $N_1$ . Thus, we assume that in the data analysis the statistical properties of the thermal noise are known (but not the particular instance that is included in the measured data). We note that it is not obvious that this noise-correction procedure, which is based on variances, applies exactly to quantiles even for non-Gaussian signals. In practice, though, we find that it works very well, and we thus conclude that this simple noise-correction property is an important advantage of working with quantiles.

The estimation in all plots was made up to redshift 27 which approximately corresponds to the SKA’s lowest measured frequency of 50 MHz. Note that the signal maps were generated with a redshift resolution of  $\Delta z = 0.1$  up to redshift 15 and  $\Delta z = 1$  above this, for all models except for the Radio model where we used resolution of  $\Delta z = 1$  for all redshifts.

### 3.4 Quantile average compared to variance

The first quantile measure we looked at is the average (in absolute value) of the high- and low-end quantiles, i.e.,

$$Q_{\text{ave}}(t) \equiv \frac{|Q_+(t)| + |Q_-(t)|}{2}. \quad (11)$$

Note that, by their definitions,  $Q_+$  is positive and  $Q_-$  is negative (not necessarily for all possible distributions, but this is the case for all realistic ones). This quantity would equal  $t$  times  $\sigma$  for a Gaussian distribution, and more generally it corresponds to estimating the distribution’s standard

deviation (except for the factor of  $t$ ). By averaging the two ends we ignore any asymmetry and get an accurate estimate of the symmetric part. As our main configuration we use a  $2\sigma$  threshold and  $R = 20$  Mpc. We could get a similar result here with the more natural  $1\sigma$ , but we prefer to keep the same choice later when we look at the difference, and that signal happens to nearly vanish for a  $1\sigma$  threshold (see Figure 8, below). Figure 4 shows the average for all five models as a function of redshift with the above main configuration parameters, with the regular standard deviation of the PDF shown for comparison. As with the quantiles, the variance estimation from the noisy map was corrected for noise by subtracting the variance of an independent noise map:

$$\sigma_{\text{est}} = \sqrt{\text{Var}(S+N_1) - \text{Var}(N_2)}. \quad (12)$$

From the plot, the quantile average accurately measures the standard deviation (times a factor of 2 in this case, i.e., our main configuration). Compared to the noise-less image, the noise-corrected estimation from the noisy map performs very well, nearly up to the highest redshifts considered, for both the quantile average and the standard deviation statistic, and for all models. The exceptions are redshifts at which the signal drops near zero for some models.

As noted above, our ability to control the threshold and smoothing radius allows us to look at different parts of the temperature distribution and at various scales (similar to what we do when using the power spectrum), and to manipulate the magnitudes of the signal and noise since smoothing affects them differently. Figure 5 illustrates the effect of using different parameter configurations for the Standard and Radio models. For high threshold and low  $R$  we get the biggest magnitude, but as can be seen for the Standard model (left panel), with this choice the estimation fails for  $z > 22$  and also becomes inaccurate below 8. The Radio model has a particularly strong signal and thus yields more accurate estimates at the highest redshifts. We conclude that having the option to control the two parameters that are varied here has the potential to yield more information from the analysis of a real dataset.

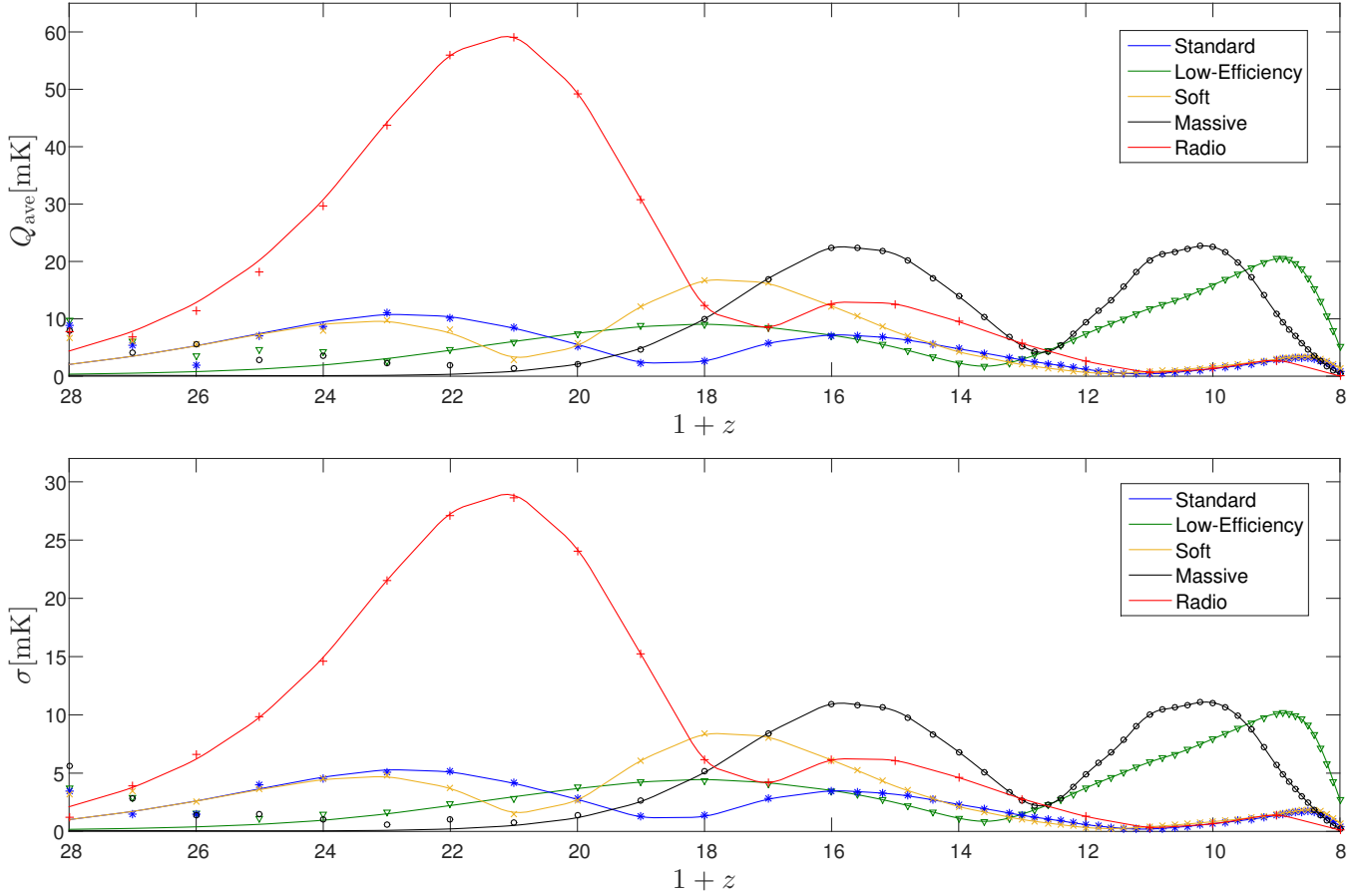


**Figure 4.** Statistics measured versus redshift, from a noise-less 21-cm image (curves) compared to the noise-corrected estimated statistics from a 21-cm image with added noise (points), with  $R = 20$  Mpc (2-D plus 3-D smoothing). Top panel: quantile average of high- and low-end  $2\sigma$  thresholds. Bottom panel: regular standard deviation of the PDF. All of our five models are shown. Note that the density of points changes according to the output redshift resolution of each simulated model.

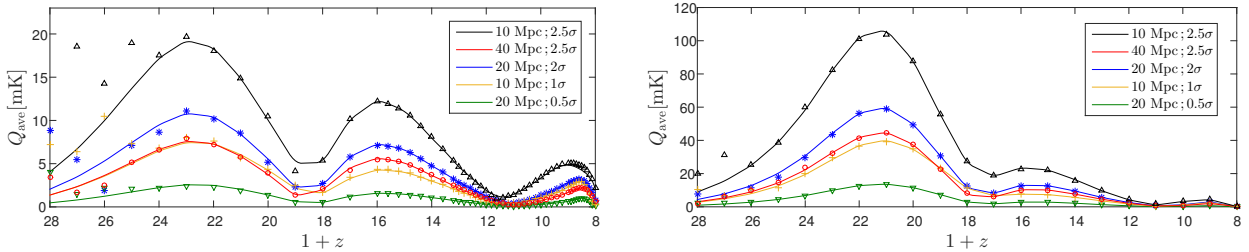


**Figure 5.** Quantile average of high- and low-end thresholds of the brightness temperature distribution as a function of redshift, for several configurations of thresholds and smoothing radii  $R$ . Left panel: Standard model, Right panel: Radio model. As in the previous figure, curves are from the noise-less signal and symbols show the estimated statistic from the map with added noise.

Most of our plots in this paper are presented as functions of redshift. However, as noted above, when we wish to select particular milestone redshifts, we define them phenomenologically using the (mock) estimated signal. Specifically, we use the redshifts where our main measure of the signal, the quantile average, achieves a peak value (i.e., a local maximum). As seen from Figure 4, from high to low redshift, in each model we have a Ly $\alpha$  peak, a Heating peak, and a Reionization peak (except that there is no Heating peak in the Massive and Low-Efficiency models).

### 3.5 Threshold dependence

The quantiles that we have defined can be used to directly compare the measured PDF to a Gaussian distribution, by varying the threshold and normalizing to a Gaussian. As the first step, we calculated the quantile-average curves (defined as in Figure 5 but for a fixed  $R = 20$  Mpc) and normalized them according to the threshold (e.g., the  $2\sigma$  curve was divided by 2). The resulting curves, shown in the top panel of Figure 6, would lie exactly on top of each other for a pure Gaussian distribution. For the simulated (noise-less) 21-cm

signal there are differences, an indication of non-Gaussianity. Note that the estimated signal from noisy maps is not plotted here since the points would be very crowded; there errors were illustrated in the previous two figures, and the normalization by a constant does not change the relative errors of the estimation.

The differences between the normalized curves are largest mostly near the cosmological milestone redshifts. We focus on these special redshifts in the other two panels. The middle panel shows the normalized quantile average at each redshift, as a function of the threshold level  $t$ . We bring out the variation more clearly in the bottom panel, where we have applied yet another normalization according to the value of each curve at the  $2\sigma$  threshold. In these two panels, a Gaussian distribution would give a flat horizontal line. The non-Gaussian signature is strongest during reionization, but all the curves exhibit interesting behavior. The symbols, which represent the same estimated statistics from the noisy signal, show that the SKA thermal noise usually does not prevent this non-Gaussianity from being measured; at the Ly $\alpha$  peak, the measurement is rather noisy in the Standard model, but the stronger signal in the Radio model allows an accurate measurement also at  $z = 20$ . Another interesting feature is that in the Radio model the curves are not monotonic as they are in the Standard model. We relate these measures of non-Gaussianity from the symmetric quantile-average to the kurtosis in section 3.7; but first we move on to the asymmetry of the positive and negative brightness temperature fluctuations.

### 3.6 Quantile difference and skewness

We now probe the asymmetry of the PDF using the difference between the high- and low-end quantiles, i.e.,

$$Q_{\text{diff}}(t) \equiv |Q_+(t)| - |Q_-(t)|. \quad (13)$$

This quantity can be compared with the standard measure of non-Gaussian asymmetry, namely the distribution's skewness given by

$$\text{Ske}(X) = \text{E}[(X - \mu)^3]/\sigma^3, \quad (14)$$

where  $\mu$  refers to the mean value of  $X$  which in our case equals zero. Both of these measures of asymmetry would equal zero for a Gaussian PDF, and cannot be probed using the 21-cm power spectrum (which measures the contribution of  $k$ -modes to the variance). Figure 7 shows our quantile difference statistic, as well as the skewness (multiplied by the measured  $\sigma(z)$  to make it have dimensions of brightness temperature), for all five astrophysical models, with the main configuration parameters ( $2\sigma$  threshold with  $R = 20$  Mpc). We see that the two statistics are quite similar (though not identical), and can be estimated accurately from a noisy map except when the signal is low at  $z > 20$ . The skewness estimation from the noisy map was done using the formula:

$$\text{Ske}_{[\text{est}]} = \frac{\text{Ske}(S+N_1)\text{Var}^{3/2}(S+N_1)}{(\text{Var}(S+N_1) - \text{Var}(N_2))^{3/2}}. \quad (15)$$

This is easily derived from the fact that the Gaussian noise has zero skewness, and the skewness of the signal is defined with respect to the variance of the (noise-less) signal.

Figure 8 shows the quantile difference for the Standard and Massive models, with various choices of threshold  $t$  and

comoving radius  $R$ . Here the signal can change sign, and is lower in absolute value than the quantile average shown earlier. Also, the shape depends more strongly on the choice of  $t$  and  $R$ . In particular, the low-threshold curves change sign compared to the high-threshold ones, and for  $1\sigma$  the signal almost vanishes. This is the reason for us choosing a  $2\sigma$  threshold (and  $R = 20$  Mpc) as our main configuration throughout this paper. Figure 8 also shows an example of the results obtained when we do not add 3-D smoothing at radius  $R$  (as discussed in section 2.2). The results for the statistic measured from the noise-less 21-cm images (the curves in the figure) are qualitatively similar to the case with 3-D smoothing, but higher in absolute value (as there is less smoothing of the 21-cm signal). However, the reconstructed signal from noisy data is significantly worse in tracing the correct signal-only result. This shows that 3-D smoothing removes thermal noise more effectively than it reduces the 21-cm signal, and justifies our inclusion of 3-D smoothing throughout this work.

### 3.7 Normalized quantile average and kurtosis

In section 3.5 we explored the threshold dependence of the quantile average. Taking the average removes the asymmetry and with it any sensitivity to the skewness of the distribution. Comparing the threshold dependence of the quantile average to a Gaussian is thus most sensitive to the kurtosis. Specifically, we take the normalized averages from the top panels of Figure 6 and divide by  $\sigma(z)$ . This quantity,  $Q_{\text{ave}}(t)/(t\sigma)$ , which for a Gaussian would equal unity (independent of  $t$ ), corresponds roughly to the distribution's kurtosis. The kurtosis is defined as

$$\text{Kur}(X) = \frac{\text{E}[(X - \mu)^4]}{\sigma^4}, \quad (16)$$

and equals 3 for a Gaussian. Figure 9 shows these two quantities for all five models as a function of redshift with the main configuration parameters ( $2\sigma$  threshold with  $R = 20$  Mpc). We chose  $t = 3$  because it gave results qualitatively somewhat more similar to the kurtosis than using  $t = 2$ . The kurtosis estimation from the noisy map was done using the formula:

$$\text{Kur}_{[\text{est}]} = \{\text{Kur}(S+N_1)\text{Var}^2(S+N_1) - \text{Kur}(N_2)\text{Var}^2(N_2) - 6[\text{Var}(S+N_1) - \text{Var}(N_2)]\text{Var}(N_2)\} / [\text{Var}(S+N_1) - \text{Var}(N_2)]^2, \quad (17)$$

which is easily derived from assuming that the thermal noise is Gaussian and independent of the signal. As before, here  $N_1$  is the thermal noise added to the signal and  $N_2$  is an independently-generated thermal noise map.

Both the kurtosis and our alternate measure can be measured accurately from noisy data up to  $z \sim 18$ . The definitions (which involve division by  $\sigma$ ) makes the kurtosis (and to a lesser degree the skewness) especially sensitive to redshifts at which the variance of the signal is particularly low (i.e., approaches zero, and becomes difficult to measure accurately). These are the points where the magnitude of the kurtosis (and of the alternate kurtosis) peaks. Examples of this can be seen at  $z = 10$  for the Standard and Soft models, where the kurtosis estimation deviates from the real signal-only curve, and at  $z > 20$  for the Massive model and  $z > 22$



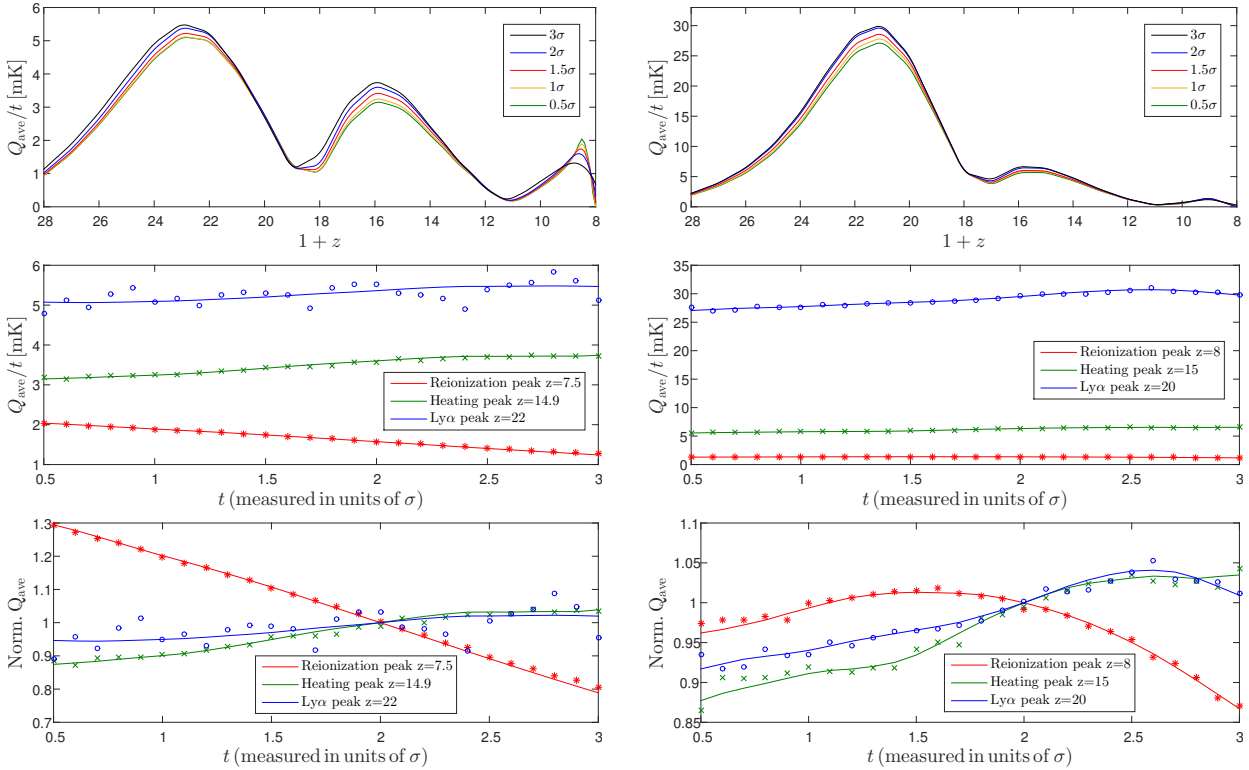


**Figure 6.** Threshold dependence of the average signal. Left panels: Standard model plots, right panels: Radio model plots. Top panels: normalized quantile average (i.e., divided by the threshold  $t$ ) as a function of redshift. Middle panels: normalized quantile average as a function of threshold for 3 milestone peak redshifts. Bottom panels: normalized (twice) curves - each curve from the middle panel was divided again by its value at threshold  $t = 2$ . Symbols in the various panels show the same plotted statistic as estimated from data with added thermal noise.

for the Low-Efficiency model. These are redshifts where  $\sigma$  approaches zero according to Figure 4.

#### 4 SUMMARY AND CONCLUSION

We have suggested quantile-based statistics as a new method for measuring non-Gaussianities in the 21-cm signal via tomography maps. This method is complementary to the global signal and power spectrum which are commonly used and not sensitive to non-Gaussian aspects such as the asymmetry of the temperature fluctuation distribution. Quantiles offer a simple, robust and flexible statistic that is easy to correct for thermal noise. Also, quantiles can be used to probe the variance, skewness, and kurtosis of the temperature distribution. The flexibility comes through the ability to choose different thresholds in the quantile measures. The robustness comes from being less sensitive to outliers than common statistics that integrate over the entire distribution function. The simplicity comes in the noise-correction, which for each quantile measure is done simply like correcting the variance, i.e., by subtracting the squares using an independent noise-only map (eq. 10).

We used mock signals from five possible astrophysical models, covering the full redshift range of the SKA and exploring a much wider range of possible signals than previous investigations of non-Gaussian statistics. This included models with different spectra of the X-ray heating sources (Soft vs. Standard model), different character-

istic masses of galactic halos (Massive vs. Standard), different star-formation and X-ray efficiencies (Low-Efficiency vs. Standard), as well as an exotic model with an excess early radio background motivated by the EDGES global 21-cm detection. To the single images we added mock thermal noise according to the expected level for upcoming observations with the SKA. We tried various smoothing/resolution radii  $R$  of the signal. Varying  $R$  allows us to explore various distance scales, similar to looking at  $k$  modes of the power spectrum. Together with the profile analysis shown in Figure 3, this can yield a broad picture of the spatial behavior of the signal and illuminate the physical processes involved. For our quantile statistics, we found it advantageous to add, as an initial analysis step, 3-D smoothing at the same radius  $R$ , as this smoothed out the noise more effectively than the signal.

We based our main statistical measures on upper and lower quantiles,  $Q_+$  and  $Q_-$ , at threshold  $t$  defined as containing a cumulative probability corresponding to a normal distribution, with  $t$  in units of  $\sigma$ . We then took the symmetric average  $Q_{\text{ave}}$  (eq. 11), which approximately corresponds to measuring the standard deviation, and the difference  $Q_{\text{diff}}$  (eq. 13), which approximately measures the skewness. We also showed that the normalized average  $Q_{\text{ave}}(t)/(t\sigma)$  approximately measures the kurtosis. The threshold dependence of  $Q_{\text{ave}}$  (Figure 6) can hold more information that might be explored. For example, we noticed a peak thresh-

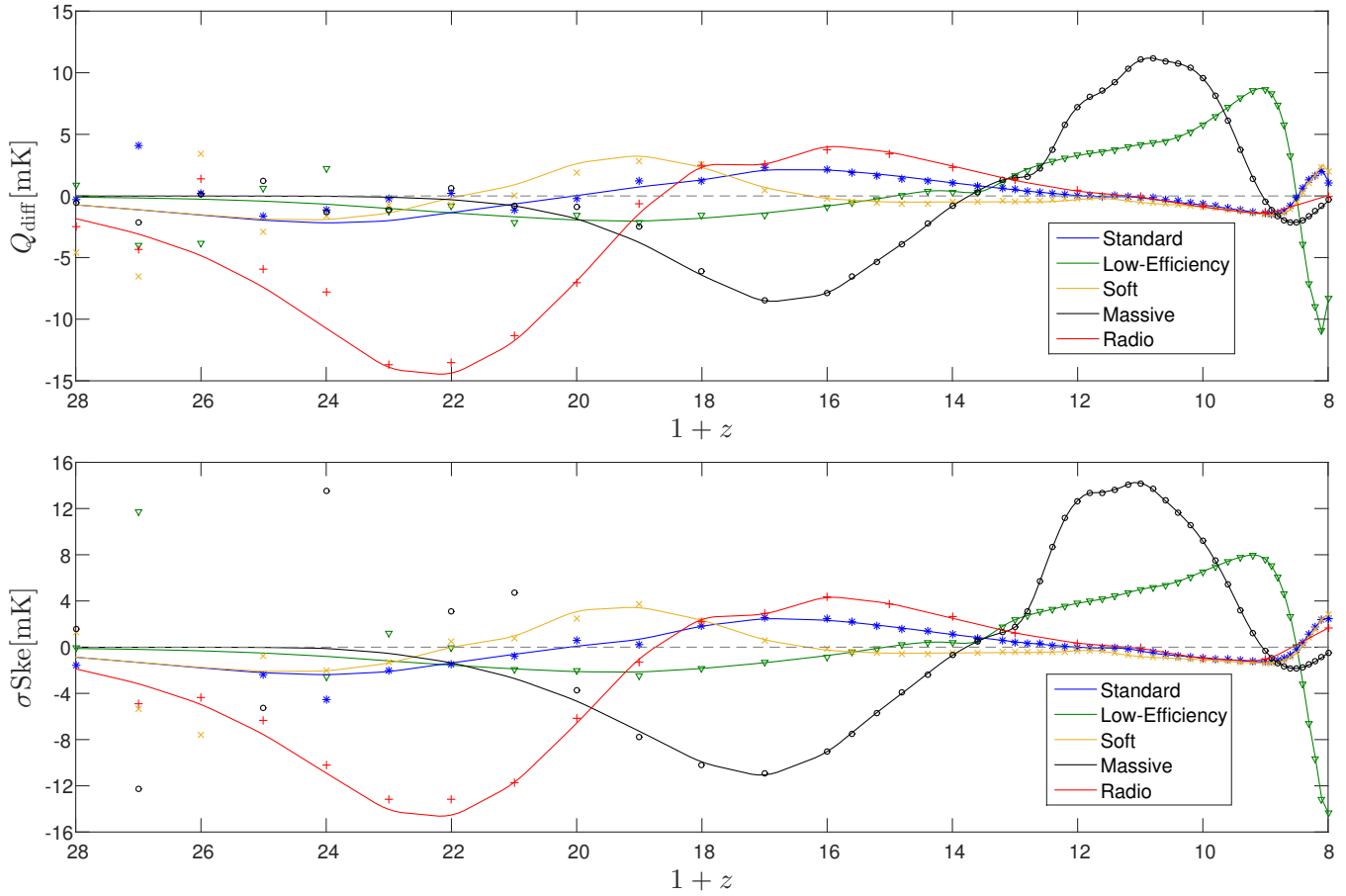


**Figure 7.** Top panel: Quantile difference of the 21-cm fluctuations using  $2\sigma$  thresholds with  $R = 20$  Mpc, shown as a function of redshift for all 5 models. Bottom panel: Skewness times  $\sigma$ , as a function of redshift, for the same five models. The symbols represent the estimated statistic in each case from the map with added noise.

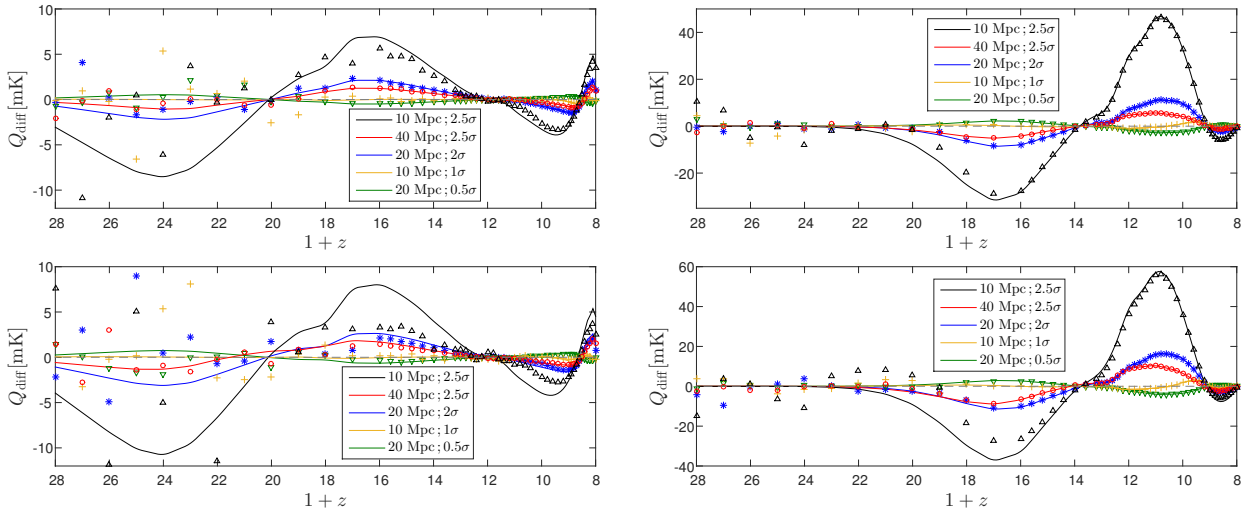


**Figure 8.** Quantile difference (as in Figure 7) as a function of redshift, for several configurations of threshold  $t$  and smoothing radius  $R$ . Left panel: Standard model, Right panel: Massive model. Top panels use 21-cm images with added 3-D smoothing as a first step of the data analysis (our default case throughout the paper, see section 2.2), while the bottom panels illustrate the same without 3-D smoothing, i.e., using “raw” images with only the inevitable 2-D smoothing that represents the observational angular resolution. Symbols in the various panels represent the estimated statistic using the map with added noise.

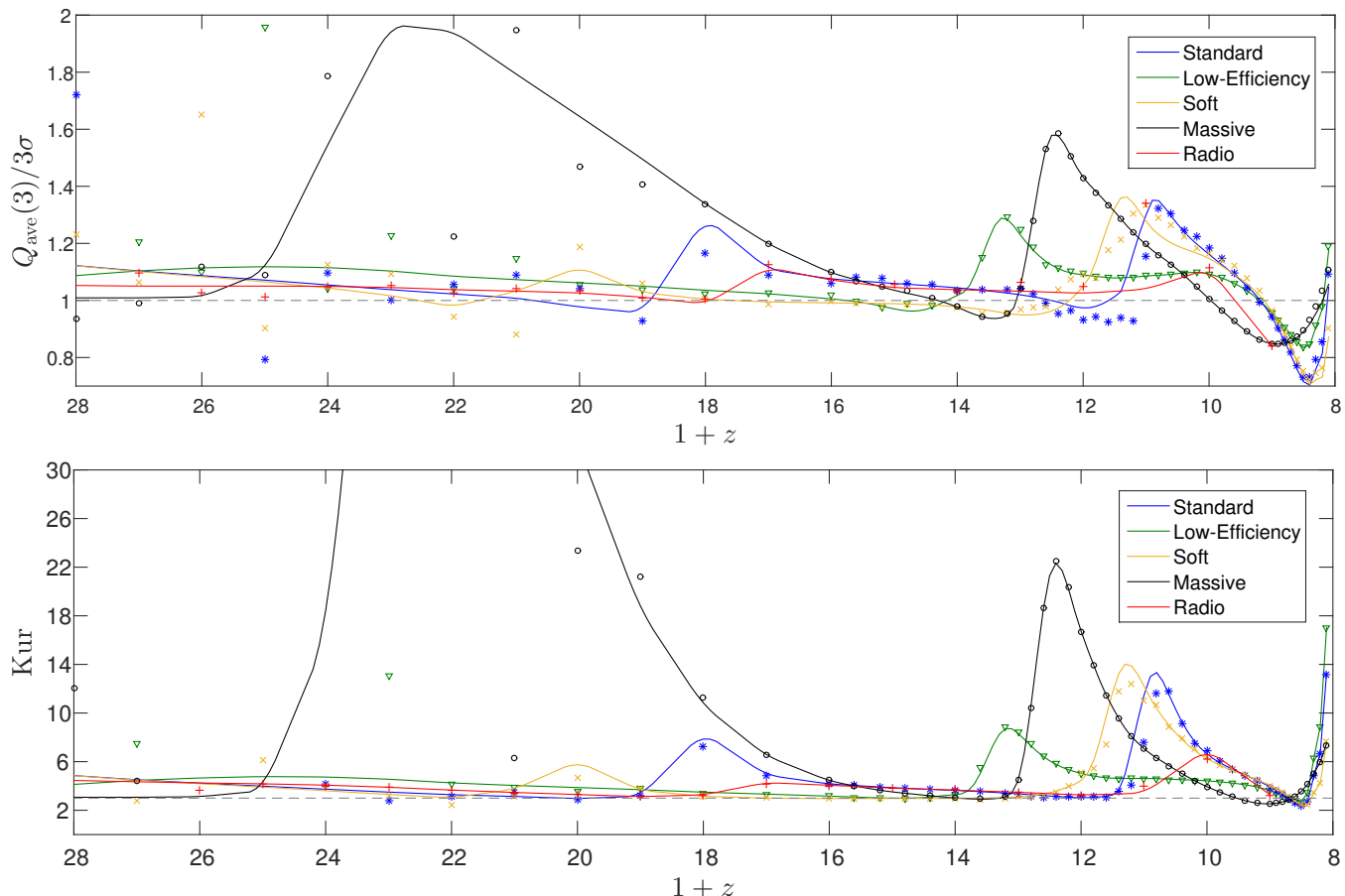


**Figure 9.** Top panel: our alternate kurtosis measure,  $Q_{\text{ave}}(t)/(t\sigma)$  with  $t = 3$  and  $R = 20$  Mpc, shown as a function of redshift for our five models. Bottom panel: kurtosis as a function of redshift. The symbols in each panel represent the same estimated statistic using the map with added noise. The horizontal gray dashed line in each panel is the corresponding value for a normal distribution. The  $y$ -axis was truncated in the bottom panel due to the fact that the kurtosis goes to infinity as the variance goes to zero (near  $z = 21$ ).

old value in the Radio model (at some redshifts) that does not appear in the Standard model.

We found that both our statistical measures and the corresponding standard measures of non-Gaussianity can be measured out to high redshift with the SKA, often out to  $z > 20$  and including the redshift of the Ly $\alpha$  peak. This was the case after accounting for the expected angular resolution and thermal noise of the SKA (i.e., SKA1-Low). This is especially true if the EDGES measurement by Bowman et al. (2018) is confirmed, as it implies a stronger amplitude of 21-cm fluctuations (as exemplified by our Radio model). Generally, each of our five different astrophysical models has a substantially different cosmic history, as measured by each statistic (all five models are shown in Figures 1, 3, 4, 7, and 9). Thus, the variation of parameters among the models shows that the minimum galactic halo mass, the star-formation and X-ray efficiencies, and the X-ray spectrum, can all be constrained if these statistics are measured.

With the SKA we will be able to directly image cosmic dawn for the first time in history. It is necessary to have a variety of methods and tools that can be applied on the collected data in order to fully extract the potential it holds. Of course, we have only taken a first step here, and the next step is to consider more realistic SKA data with foreground

residuals. We expect that the flexibility and robustness of the quantile statistics will help to deal with that as well. On the optimistic side, we note that we have used here a simulation box with volume approximately equal to that of a single SKA field, while SKA observations will create large surveys covering multiple fields. Thus, 21-cm cosmology with the SKA holds great promise.

## 5 ACKNOWLEDGMENTS

This project/publication was made possible for AB and RB through the support of a grant from the John Templeton Foundation. The opinions expressed in this publication are those of the authors and do not necessarily reflect the views of the John Templeton Foundation. AB and RB were also supported by the ISF-NSFC joint research program (grant No. 2580/17). AF was supported by the Royal Society University Research Fellowship.

## REFERENCES

- Barkana, R., 2016, PhysRep, 645, 1
- Barkana, R., 2018, Nature, 555, 71

- Barkana, R., Loeb, A., 2005, *ApJ*, 626, 1
- Bharadwaj, S., & Pandey, S. K., 2005, *MNRAS*, 358, 968
- Bowman, J. D., Rogers, A. E. E., Monsalve, R. A., Mozdzen, T. J., Mahesh, N., 2018, *Nature*, 555, 67
- Ciardi B., Madau P., 2003, *ApJ*, 596, 1
- Cohen, A., Fialkov, A., Barkana, R., Lotem, M., 2017, *MNRAS*, 472, 1915
- Feng, C., Holder, G., 2018, *ApJ*, 858, 17
- Fialkov, A., Barkana, R., 2019, *MNRAS*, 486, 2, 1763
- Fialkov, A., Barkana, R., & Visbal, E., 2014, *Nature*, 506, 197
- Field, G. B. 1958, *PIRE*, 46, 240
- Fragos T., Lehmer B. D., Naoz S., Zezas A., Basu-Zych A., 2013, *ApJL*, 776, L31
- Furlanetto S. R., Zaldarriaga M., Hernquist L., 2004, *ApJ*, 613, 16
- Harker G. J. A., et al., 2009, *MNRAS*, 393, 1449
- Ichikawa K., Barkana R., Iliev I. T., Mellema G., Shapiro P. R., 2010, *MNRAS*, 406, 2521
- Kittiwisit P., Bowman J. D., Jacobs D. C., Thyagarajan N., Beardsley A. P., 2016, *arXiv*, arXiv:1610.06100
- Koopmans, L., et al., 2015, *Advancing Astrophysics with the Square Kilometre Array*, PoS(AASKA14)001
- Kubota K., Yoshiura S., Shimabukuro H., Takahashi K., 2016, *PASJ*, 68, 61
- Madau P., Meiksin A., Rees M. J., 1997, *ApJ*, 475, 429
- Majumdar S., Pritchard J. R., Mondal R., Watkinson C. A., Bharadwaj S., Mellema G., 2018, *MNRAS*, 476, 4007
- Mellema G., Iliev I. T., Pen U.-L., Shapiro P. R., 2006, *MNRAS*, 372, 679
- Mesinger A., Furlanetto S., Cen R., 2011, *MNRAS*, 411, 955
- Mineo, S., Gilfanov, M., Sunyaev, R., 2012, *MNRAS*, 419, 2095
- Mirabel, I. F., Dijkstra, M., Laurent, P., Loeb, A., Pritchard, J. R., 2011, *A&A*, 528, 149
- Mondal R., Bharadwaj S., Majumdar S., Bera A., Acharyya A., 2015, *MNRAS*, 449, L41
- Pritchard, J. R., Furlanetto, S. R., 2007, *MNRAS*, 376, 4, 1680
- Pritchard, J. R., Loeb, A., 2012, *Reports on Progress in Physics*, 75, 086901
- Shimabukuro H., Yoshiura S., Takahashi K., Yokoyama S., Ichiki K., 2015, *MNRAS*, 451, 467
- Trott C. M., et al., 2019, *PASA*, 36, e023
- Watkinson C. A., Pritchard J. R., 2014, *MNRAS*, 443, 3090
- Watkinson C. A., Pritchard J. R., 2015, *MNRAS*, 454, 1416
- Wouthuysen, S. A. 1952, *AJ*, 57, 31
- Wyithe J. S. B., Morales M. F., 2007, *MNRAS*, 379, 1647